Electrochimica Acta 430 (2022) 141106

Contents lists available at ScienceDirect

Electrochimica Acta

journal homepage: www.journals.elsevier.com/electrochimica-acta

# Supercapacitor and oxygen evolution reaction performances based on rGO and $Mn_2V_2O_7$ nanomaterials

E.A. Kamar [a], K.F. Qasim [b,*], M.A. Mousa [a]

[a] Chemistry Department, Faculty of Science, Benha University, Benha, Egypt
[b] Chemistry Department, Faculty of Science, Suez University, Suez, Egypt

ARTICLE INFO

*Keywords:*
Supercapacitor
rGO
$MnV_2O_7$
Composite
Electro-catalysis

ABSTRACT

Manganese vanadate $Mn_2V_2O_7$ (MVO), and reduced graphene oxide (rGO) have been synthesized for supercapacitors and electrocatalytic applications. The structure and electrochemical characterization studies were performed by several techniques, including XRD, SEM, TEM, XPS, BET, cyclic voltammetry (CV), Linear sweep voltammetry (LSV), galvanostatic charge-discharge (GCD), and electrochemical impedance spectroscopy (EIS). The characterization tools of the investigated samples showed an amorphous structure for rGO and a monoclinic structure for MVO. The single electrodes of the investigated samples showed a specific capacitance of 120, 235, and 330 F/g for rGO, MVO, and rGO@MVO, respectively, in an electrolyte of 1M of $LiClO_4$ in propylene carbonate solution. The electrochemical behavior of an asymmetric supercapacitor (ASC) of rGO@MVO//AC was studied under a potential window of 0–2 V, providing a high energy density of 66.6 Wh $kg^{-1}$ at a power density of 19478 W $kg^{-1}$. The ASC cell showed a specific capacitance of 112 F/g at a current density of 10 A/g and cycling stability with 86.6% capacitance retention over 8000 cycles. For oxygen evolution reaction, the rGO@$Mn_2V_2O_7$ electrode showed a lower overpotential of 225 mV at a current density of 10 mA $cm^{-2}$, with a Tafel slope of 54 mV $dec^{-1}$, displaying a fast and effective reaction rate. These outcomes indicate that rGO@$Mn_2V_2O_7$ can be used as hopeful electrode material for supercapacitor and water splitting applications.

## 1. Introduction

With the speedy improvement of human civilization, the requests for energy reserves have become very imperious [1–3]. Presently, energy is mainly obtained from conventional fossil fuels [4–6]. However, they might produce dangerous environmental pollution, so it is essential to search for other clean energy resources to resolve the problem. This can be done through wind power and photovoltaics (PVs). However, they are highly fluctuating on many different time scales. Therefore, one of the most important future challenges for the stability of the desired supply grid based on renewable energies will be controlling and suppressing these fluctuations [7–9]. So far, electro-catalysis of water and supercapacitors is considered a potential technology to get conversion and storing energy. Firstly, the supercapacitor is one of the current devices for energy storage due to its low fabricating cost, long cycle stability, high power density, and distinctive rate capacity [10–13]. Secondly, electro-catalytic water splitting is a globally approachable way of creating oxygen and hydrogen for the source of clean fuels, which could lessen the energy emergency [14–19]. The water-splitting procedure is organized into two processes: hydrogen evolution reaction (HER) and oxygen evolution reaction (OER) [20,21]. Nevertheless, water splitting reactions are affected by slow kinetics,

*Abbreviations:* AC, Activated Carbon; ASC, asymmetric supercapacitor; C, specific capacitance of electrode; $C_{dl}$, electrochemical double-layer capacitance; $C_{SP}$, specific capacitances; CV, cyclic voltammetry; $D_{XRD}$, Particle Size; $E_{CSA}$, electrochemical active surface area; $E_d$, energy density; EDLCs, electrical double-layer capacitors; EIS, electrochemical impedance spectroscopy; ESR, equivalent series resistance; GCD, galvanostatic charge-discharge; GCEs, Glassy carbon electrodes; GO, Graphene Oxide; HER, hydrogen evolution reaction; i, response current; LiTFSI, Li-)bistrifluoromethanesulfonylimide; LSV, Linear sweep voltammetry; m, mass of the active material; MVO, Manganese vanadate $Mn_2V_2O_7$; OER, oxygen evolution reaction; $P_d$, power density; $R_{CT}$, charge transfer resistance; rGO, reduced graphene oxide; rGO@MVO, Composite; $R_s$, solution resistance; SEM, scanning electron microscopy; TEM, Transmission electron microscopy; V, potential window; $W_D$, Warburg resistance; XPS, X-ray photoelectron spectroscopy; XRD, X-ray diffraction; XRF, X-ray fluorescence; Δt, discharge time; η, overpotential; υ, potential scan rate.

* Corresponding author.
*E-mail address:* Khaled.Faisal@sci.suezuni.edu.eg (K.F. Qasim).

https://doi.org/10.1016/j.electacta.2022.141106
Received 20 April 2022; Received in revised form 26 August 2022; Accepted 26 August 2022
Available online 28 August 2022

considerable over-potential, and inadequate energy efficiency rising from difficult courses of electrons/ions transport in OER and HER [22]. It is broadly recognized that the OER course, which has a significant energy barrier, is more kinetically slow than HER and thus extremely restricts the suitable employment of general water splitting [23]. Furthermore, oxygen evolution reaction plays a critical part in several other energy-storing techniques like fuel cells, and metal-air batteries [24]. To date, electro-catalysts have been used to promote OER kinetics [25]. These catalysts decrease the over-potential needed for water splitting. Some precious metals, e.g., Ir, Pt, and Ru have been used as electro-catalysts in the water-splitting process owing to their high activity, super durability, and low over-potential values [26]. But, their high price, limited obtainability, and instability in basic media at high current density considerably inhibit their significant industrial applications [27,28]. These drawbacks can be raised above by using a high-performance OER electro-catalyst of non-precious metals with low price, distinguished effectiveness, and stability [29,30]. In these situations, notable achievements have been attained in transition metal-based OER electro-catalysts, particularly Fe, Co, Ni [31,32], and their oxides [33,34], and selenides [35,36], sulfides [37,38], nitrides [39,40], borides [41,42], carbides [43,44], and organometallic compounds [45,46].

Presently, the supercapacitor contains two electrodes, an electrolyte (aqueous, organic, ionic liquid, or solid), and a separator that can be used as an effective energy storage device. The electrodes either be the same for the symmetric supercapacitor (SCs) or dissimilar for asymmetric supercapacitors (ASCs) [47]. There are two classes of supercapacitors: electrical double-layer capacitors (EDLCs) and pseudocapacitors [48,49]. In the first one, EDLCs, the energy is stored across the collection of the charges on the boundary between the electrode and electrolyte. In the second type, pseudocapacitors, the energy is stored throughout a rapid and reversible faradaic redox reaction [50, 51]. Generally, the pseudocapacitor submits a higher energy density than that double-layer capacitor due to the transportation of a large quantity of the charges in the faradaic process [52]. Currently, the modest energy density is the bottleneck of supercapacitors [53,54]. Therefore, the researchers try to improve a supercapacitor's energy density by expanding the potential window and employing an electrode material with high capacitance [55,56].

As the core parts of the two technologies mentioned above, the design and improvement of cheap, very active, and durable materials are central to supporting the reasonable use of electro-catalytic water splitting and supercapacitors [57].

The presented literature states that mixed transition metal oxides such as ferrites and vanadates comparable to the analogous monometallic oxides have better electrochemical activity due to the multiple valence states and a considerable quantity of active sites, especially when they are present in nanosized states [58,59]. $Mn_2V_2O_7$, as one of these transition metal vanadates, has low conductivity; therefore, to be used in supercapacitors and electro-catalytic applications, they should be modified by adding a high conductive material such as graphene and its derivatives. This study synthesized and studied the electro-catalytic and supercapacitors' efficiency of nano-$Mn_2V_2O_7$ and its composite with rGO.

## 2. Experimental

### 2.1. Materials

Ammonium monovanadate extra pure ($NH_4VO_3$) (Oxford, India), manganese chloride tetrahydrate extra pure ($MnCl_2.4H_2O$) (Oxford, India), and Ethanol ($C_2H_5OH$) 99% (Adwic Pharmaceutical and Chemicals Company, Egypt). Activated carbon (AC) with a surface area of 1100 $m^2/g$ was supplied from Jiangsu Zhuxi Activated Carbon Co., Ltd. Lithium bis(trifluoromethanesulfonyl)imide (LiTFSI) (99.9%, 3M) was employed as an electrolyte and supplied from Sigma Aldrich, USA. All the other materials are of analytical grade and were used as received.

### 2.2. Preparation of rGO

Graphene Oxide (GO) was firstly synthesized by oxidizing graphite powders according to the Hummer method [60]. Graphite powder (5 g) was mixed with concentrated sulfuric acid ($H_2SO_4$, 115 ml, 98 wt%, in a 500 ml glass beaker putting in an ice bath). Then 2.5 g of $NaNO_3$ was inserted into the solution, and 20 g of $KMnO_4$ was gradually added with continuous vigorous stirring for 2 h at temperatures below 10 °C, followed by 1 h at 35 °C. After that, 250 ml of de-ionized water was added to the reaction. After ending the effervescence, the suspended solution was heated up to 98 °C and kept for 10 min before cooling it to room temperature. After that, 50 ml of $H_2O_2$ were inserted into the suspended solution, heated up to 90 °C, and kept for half an hour. The suspension was filtered and washed five times with a large quantity of boiling water until the supernatant water approached neutral pH. Lastly, the produced GO was dried at 60 °C for 24 h. To prepare rGO, 0.2 g of the dry GO was dispersed in 100 ml de-ionized water and sonicated for 40 min, then heated up to 98 °C by adding 6 ml hydrazine hydrate and kept at 98 °C for 24 h. The resultant black product was gathered by centrifugation at 4000 r/s, washed with distilled water five times to eliminate the excess hydrazine, and dried at 120 °C for 24 h.

### 2.3. Preparation of manganese vanadate

9.6 mmol manganese chloride (1.899 g) was dissolved into 160 ml of de-ionized water. 9.6 mmol ammonium monovanadate (1.123 g) was dissolved into 80 ml of de-ionized water at 60 °C and added slowly to the manganese chloride solution under continuous vigorous stirring for 15 min. After the additive was completed, the resultant suspension was put in a 300 ml Teflon-lined stainless autoclave and kept at 210 °C for 24 h, followed by cooling down to room temperature. The suspended solution was then centrifuged at 4000 r/s, and the produced powder was washed five times with de-ionized water and ethanol, then dried at 75 °C for six hours. The powder produced was calcined at 450 °C for three hours in the air and labeled as MVO.

### 2.4. Preparation of rGO@MVO nanocomposite

1.05 g of the synthesized rGO was inserted into 125 ml de-ionized water and dispersed by sonication for one hour; then, 2 g MVO was inserted into the suspension with stirring for two hours. The suspended solution was then put into a 250-ml Teflon-lined autoclave and heated to 125 °C for seven hours. Lastly, the autoclave was set aside to cool to 25 °C, and the produced powder was washed 5 times with bi-distilled water, dried, and denoted as rGO@MVO.

### 2.5. Characterization

The investigated samples' X-ray diffraction (XRD) patterns were measured using Bruker AXS D8 Advance X-ray diffractometer with Cu radiation ($\lambda = 1.5406$ Å). All the samples were exposed to the radiation with step scan 0.02 in 2 h in the range of $2\theta = 5–80^o$ with a primary beam power of 40 kV and 35 mA. The constituent elements and the elemental ratio were analyzed using X-ray fluorescence (XRF) Bruker; model: S4 PIONEER). The samples were ground into a fine powder, and a pressed pellet was prepared using boric acid as a binder under a hydraulic pressure of 10 metric tons before analysis. The morphology of the samples was analyzed using scanning electron microscopy (SEM) JSM-IT200. Further examination of morphology was accomplished through TEM images taken by the JEOL-2010 TEM instrument, functioning at the accelerating voltage of 120 kV. TEM samples were prepared by crushing a sample in an agate mortar in ethanol and depositing the obtained suspension on a copper carbon holey grid. The surface properties were analyzed via $N_2$ adsorption/desorption at 77 K by the

volumetric technique via Belsorp-mini II (Japan) surface area analyzer. The pores size was calculated using BJH (Barrett-Joyner- Halenda) method from the adsorption isotherms. X-ray photoelectron spectroscopy XPS was carried out on an ultra-high-vacuum K-ALPHA (Thermo Fisher Scientific, USA) spectrometer. Non-monochromatized Al Ka exciting X-ray radiation was used. For the experimental setup, the emission was at 10 mA, the anode (HT) was 15 kV, and the pressure for the analysis chamber was $5 \times 10^{-9}$ torr.

### 2.6. Electrochemical and electro-catalyst measurements

Electrochemical measurements were carried out in a typical three-electrode cell using an electrolyte of 1M of $LiClO_4$ in propylene carbonate solution, using Pt square foil (area=0.59 $cm^2$) as a counter electrode, and saturated calomel as a reference electrode. The working electrodes were made by mixing 8 mg of the investigated samples, 1 mg of acetylene black, and 1 mg of polytetrafluorethylene (5% wt) to form a homogeneous slurry; coated onto FTO glass. The one mm formed a thick layer of vanadate materials was covered with Nafion membrane (obtained by dissolving a commercial Nafion solution 9/1 v/v in ethanol) to prevent the material's degradation into the electrolyte solution. The electrode was then dried for 3 h at RT. The loading amounts of catalysts range between 0.21–0.25 mg $cm^{-2}$. The electrochemical activity of the prepared electrodes was analyzed on an electrochemical workstation (CHI 660e) using the CV and GCD measurements. The EIS analysis was skillfully guided through an open-circuit potential at frequencies ranging from $10^{-2}$ to $10^5$ Hz. The electrochemical characterizations of an asymmetric supercapacitor (ASC) consisting of rGO@MVO as a positive electrode and activated carbon (AC) as a negative electrode was studied using a two-electrode pneumatic coin cell. The circular electrodes (1 $cm^2$) were pressed together in the coin cell and separated by an electrolyte membrane of LiTFSi-soaked PTFE.

In water-splitting experiments, 1 M KOH aqueous solution was employed as the electrolyte, a platinum wire as the counter electrode, and catalyst-coated Glassy carbon electrodes (GCEs) with a diameter of 5 mm as the working electrode. Firstly, the GCE was mechanical polished with leather containing 0.05 μm $Al_2O_3$ and then washed in ethanol and distilled water. The GCE was then sonicated in de-ionized water for 15 min to remove alumina adsorbed on the electrode surface. Inks of the synthesized catalytic materials ((MVO or rGO@MVO) were prepared by sonicating dispersed solutions composed of 5 mg of the catalyst, 1 ml mixed solution of de-ionized water, and ethanol (1:1 in volume ratio), and 15 μL 6 wt% Nafion solution. 10 μL of the prepared ink was then pipetted on top of GCE. Finally, the catalyst-coated GCE was dried in air at RT. The electrochemical cell was purged with $O_2$ for 20 min to saturate the electrolyte, and the $O_2$ flow was continued over the solution during the test. Electro-catalytic measurements were performed using the linear sweep voltammetry (LSV) technique within a potential range from 1.22 V to 1.85 V vs. RHE and a sweep rate of 10 mV $min^{-1}$. All the measured potentials were changed to the scale of reversible hydrogen electrode (RHE) using the equation: $E_{RHE} = E_{SCE} + 0.242 + 0.059$ pH [61]. The over-potential (η) for the OER was calculated using the equation: $\eta = E_{RHE} - 1.23$. The stability of the electrode was examined by chronopotentiometry at a current density of 10 mA/$cm^{2+}$. Electrochemical impedance spectroscopy (EIS) was done in the frequency range between $10^{-1}$ to $10^3$ Hz with an applied AC amplitude of 10 mV.

## 3. Results and discussion

### 3.1. X-ray diffraction analysis

Fig. 1 shows XRD peaks characterized for the investigated materials. The reduced graphene oxide (rGO) demonstrates broad reflection peaks at $2\theta = \sim 24^\circ$ and $42^\circ$, matching d-spaces of 0.37 and 0.21 nm, suggestive of restacking to produce a defectively ordered graphite-like material [62]. $Mn_2V_2O_7$ shows a monoclinic phase structure according to JCPDS 22-436. The XRD of the binary system rGO@MVO shows peaks agreeing with the XRD data of all the constituent materials. The peak emerging at 42.71° corresponding to the (100) plane of rGO authorizes its presence in the binary system. Moreover, a decrease observed in the peak intensities of MVO in the spectrum of rGO@MVO refers to coating rGO on the MVO surface. Moreover, the angles of the peaks characterized for MVO phases (021) and (-201) are slightly shifted, referring to some interactions between rGO and MVO.

### 3.2. XPS analysis

The XPS technique was employed to examine the sample purity and to establish the quantitative constitution. The scan XPS for the MVO@rGO sample is illustrated in Fig. 2a, which shows the main elements of the sample (Mn, V, C, O), besides traces of the N elements. The XPS analysis results showed the atomic ratio of 1: 1:1 MVO for Mn:V: C, which matches with XRF data and the composition of the starting materials. The N element is produced through the reduction process of GO to rGO by hydrazine hydrate [63]. As the binding energy of the core levels of the elements present in the sample depends on the element's oxidation state, high XPS resolution spectra for V, Mn, C, and O were analyzed to detect the different oxidation states present in the sample. The results obtained are given in Fig. 2 b-e. The high-resolution XPS spectrum of the Mn 2p peak, Fig b., shows the presence of spin-orbit

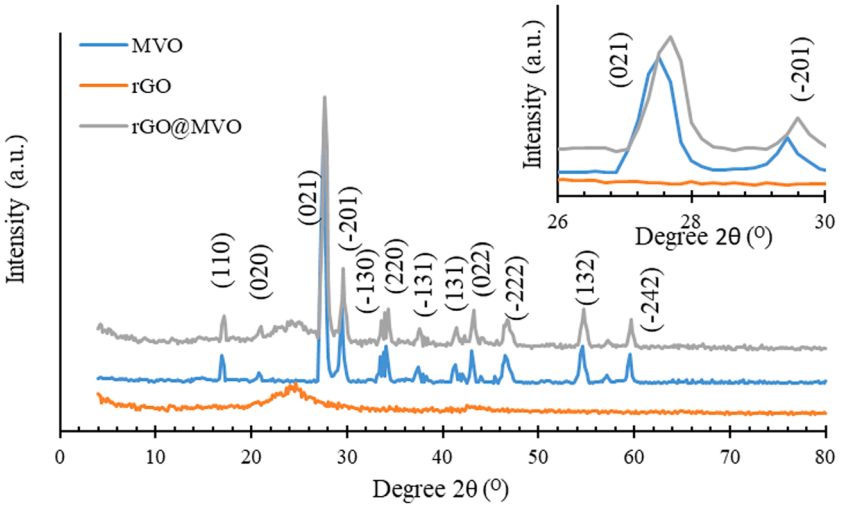


**Fig. 1.** XRD of the investigated samples.

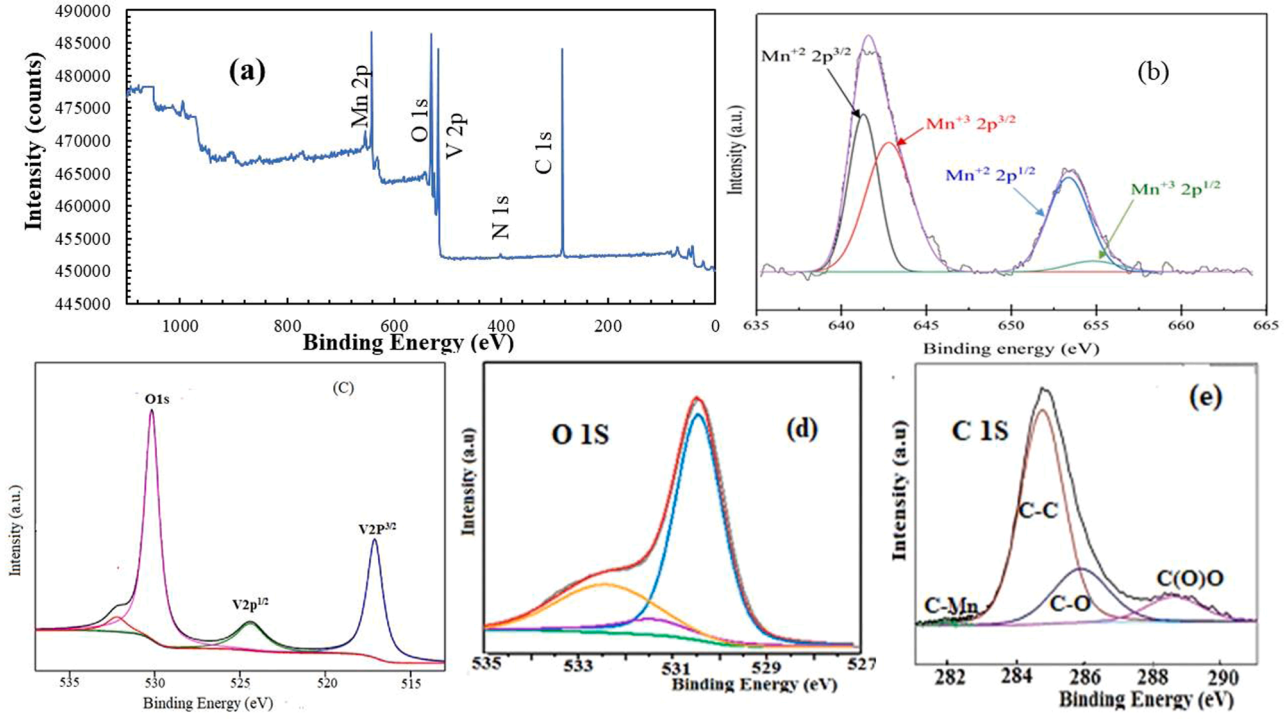


**Fig. 2.** XPS spectra of rGO@$Mn_2V_2O_7$ a survey spectrum, (b) high-resolution Mn 2p, (c) high-resolution V 2p, (d) high resolution O1s and high resolution C 1s.

splitting in two possible states, 3/2 and 1/2, with different binding energies, at 642.1 eV and 654.1 eV, respectively [64], matching with binding energies of $Mn^{2+}$ and $Mn^{3+}$ species [65]. The V 2p peaks appearing at 516.8 eV and 524.5 eV, Fig 2c., are assigned to $2p^{3/2}$ and $2p^{1/2}$ electronic states of V ions, respectively [66,67]. The oxidation state of the vanadium ion can be decided by the difference in binding energy (Δ) between the O1s and $V2p^{3/2}$ levels [67]. Our work's acquired Δ ($V2p^{3/2}$-O1s) value is 13.9 eV, which coincides with the registered value of $V^{4+}$ compounds in the literature [68].

The O 1s XPS signal is divided into three peaks for MVO at 529.9, 530.7, 531.9 eV, Fig. 2d. Nonetheless, the accurate appointment of the higher binding energy peaks is not easy and contentious as several factors such as surface defects, impurities, or chemisorbed oxygen species could cause the development of the shoulder peaks [69,70]. The investigation of carbon states (Fig. 5b) demonstrates the existence of four modes of carbon bonds that is C—V (282.1 eV), C—C (284.7 eV), C— O (287.9 eV), and COO (288.7 eV).

### 3.3. Surface study

It is well known that the high specific surface area and the uniform mesoporous structure of the materials play significant roles in developing their electrical properties and electrochemical applications [71]. Therefore, the textural properties of the investigated samples were studied by $N_2$ adsorption/desorption isotherm measurements performed at 77 K, and the acquired outcomes are represented in Fig. 3. The figure shows that all samples have hysteresis loops with capillary condensation at $P/P^\circ > 0.45$ for rGO and $P/P^\circ > 0.85$ for $Mn_2V_2O_7$ and

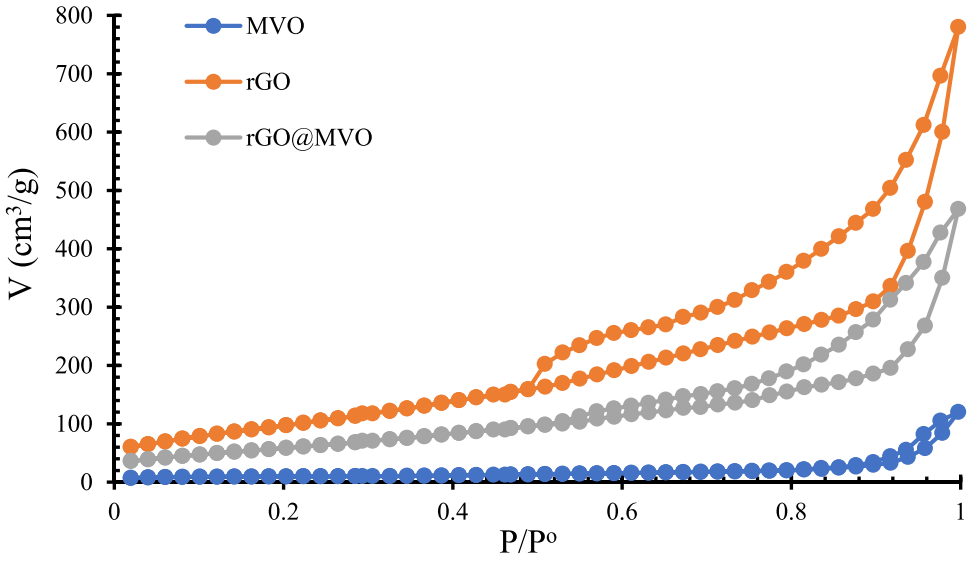


**Fig. 3.** $N_2$ adsorption-desorption isotherm of the investigated materials.

rGO@$Mn_2V_2O_7$. The observed hysteresis loops of the rGO match with adsorption of type V with H3 characteristics according to the IUPAC classification and refer to the mesoporous structures. The adsorption is attached to a weak interaction between the adsorbate and the adsorbent materials with the aggregates of the plate-like particles accumulated into slit-like pores. Conversely, the hysteresis loops of $Mn_2V_2O_7$ and rGO@$MnV_2O_7$ samples can be better described by the type V with H1 distinguishing for a high degree of pore size uniformity. The specific surface area ($S_{BET}$) calculated by the BET equation [72] and the average Barrett–Joyner–Halenda pore size ($d_{BJH}$) using the desorption data are listed in Table 1. The table demonstrates that the $S_{BET}$ of the investigated materials increases in the order: of rGO > rGO@$Mn_2V_2O_7$ > $Mn_2V_2O_7$. Whereas the $d_{BJH}$ increases according to rGO@$Mn_2V_2O_7$ > rGO > $Mn_2V_2O_7$ (Table 2).

### 3.4. SEM and TEM analysis

The SEM and TEM micrographs of the investigated samples are shown in Fig. 4. The SEM (Fig. 4a) and TEM (Fig. 4d) images of rGO show fiber structures with average diameters of 10 nm. The SEM (Fig. 4b) and TEM (Fig.4 e) images of MVO demonstrate rod shapes. The images of the binary system rGO@$Mn_2V_2O_7$ (Fig. 4c and f) demonstrate covering $Mn_2V_2O_7$ nanorods by sheets of rGO nanofiber accompanied by a considerable shrinkage in the fiber lengths.

### 3.5. Supercapacitance

The supercapacitor characteristics of rGO, $Mn_2V_2O_7$, and rGO@$Mn_2V_2O_7$ electrodes were studied using CV, GCD, and EIS techniques in 1M $LiClO_4$ electrolyte within a potential range (-0.2–1.0 V *vs.* SCE). The CV voltammograms of all samples at a scan rate of 10 mV $s^{-1}$ are demonstrated in Fig. 5a. The CV curve of rGO displays nearly rectangular cyclic voltammograms referring to an electrochemical behavior of the EDL supercapacitor [73]. The CV plot of the pure $Mn_2V_2O_7$ shows two peaks generated by reversible redox reaction, recommending a pseudocapacitance behavior generated from the redox reaction of several vanadium oxidation states. The CV voltammogram of the rGO@$Mn_2V_2O_7$ electrode demonstrates inadequate symmetry with modest redox peaks, which comprise surface adsorption and the electrolyte cations incorporation [74].

The specific capacitances ($C_{SP}$) of the working electrodes were computed from CV curves using Eq. (1) [75].

$$C_{sp} = \frac{1}{2mv\Delta V}\int_{-V}^{+V} iVdV \quad (1)$$

where i is the response current (A), ΔV is the potential window (V), m is the mass of the active material (g), and $\nu$ is the potential scan rate ($mVs^{-1}$). The obtained values are listed in Table 3, which demonstrates that the $C_{sp}$ of the rGO@$Mn_2V_2O_7$ composite is higher than that of its constituent. Therefore, the CV of the composite sample is investigated at several scan rates and the curves obtained are shown in Fig. 5b, which illustrates that the shapes of the CV plots did not change at the high scan rate, indicating the outstanding stability and charge storing characteristics for the electrodes still at the highspeed charge-transfer course. Fig. 5b also shows that the currents increase with the rise in the scan rate [76]. However, the $C_{sp}$ values decreased by increasing the scan rate. This behavior can be interpreted by simple diffusion and fast mobility of the $Li^+$ ions towards the active electrode material. At the lower scan rate, the $Li^+$ ions of the electrolyte can utilize the most accessible sites on the surface of the electrode because the $Li^+$ has sufficient time to diffuse into all the sites producing higher capacitance. On the contrary, at the higher scan rates, the $Li^+$ ions meet problems catching all the reachable locations on the active electrode surface owing to their limited transfer rate in the electrolyte. Subsequently, at higher scan rates, several active divisions of the electrode surface areas become inaccessible for charge storage.

**Table 1**
XRD, TEM, and $N_2$ adsorption data of the investigated samples.

| Sample | $D_{XRD}$ (nm) | $D_{TEM}$ (nm) | Surface area $m^2/g$ | Pore Size nm |
|---|---|---|---|---|
| rGO | 7.2 | nanosheet with a diameter of, 10 nm | 312.7 | 4.1 |
| MVO | 30 | rods with average diameters of 20 and lengths of 120 nm | 16.5 | 3.9 |
| rGO@MVO | 22 | nanofiber rGO sheets covered MVO nanorods (aver. diameter of rGO 7 nm and rods (aver., diameters 8 nm and lengths 50 nm) | 277.8 | 4.3 |

**Table 2**
Binding energies (eV) of the elements of $Mn_2V_2O_7$@rGO.

| | | |
|---|---|---|
| Mn | $2p^{3/2}$ | 642.4 |
| | $2p^{1/2}$ | 645.1 |
| V | $2p^{3/2}$ | 516.7 |
| | $2p^{1/2}$ | 524.5 |
| C | 1s | 284.4, 285.9, 288.7 |
| O | 1s | 530.5, 532.5, 531.4 |

The performance in capacitance of composite material (Table 3) may be attributed to the presence of a large quantity of the rGO with a high surface area, a high number of mesopores, and a high conducting network. The presence of rGO during the preparation of the composite sample can provide sites for minute crystal growth of MVO without any aggregation. The small size guarantees the appropriate activation of active materials during reactions. Moreover, such a framework structure would enable electrolytes to access the internal surface and enhance the electron transference for the period of the charge and discharge progresses, consequently developing the electrical conductivity and charge transfer paths generated in pure $Mn_2V_2O_7$. The non-rectangular category of the CV voltammograms and the display of peaks at higher scan rates inform the departure from the ideal trend and the meaningful participation of pseudocapacitance to the total specific capacitance. This performance may be ascribed to that the $Li^+$ ions do not have sufficient time to introduce the multilayered body of the electrode and generate a collection of charges at the interface [77].

The GCD studies of the studied electrodes conducted at a current density of 1 A/g are presented in Fig. 5c. Contrary to the rGO electrode, the discharge plots of $Mn_2V_2O_7$ and binary composite electrodes show a deviation from linearity due to their pseudo-capacitance behavior. All discharge plots have an internal resistance drop (IR-drop) recognized as the equivalent series resistance (ESR), which contains all the resistances of the cell (electrode, electrolyte, contact resistance) [78]. The ESR values follow the order of MVO > rGO@MVO > rGO. The decrease in the ESR value of the composite to that of $Mn_2V_2O_7$ has been attributed to the existence of conducting rGO in the composite, which forms a speedy electron transportation path in the composite electrode. The specific capacitances of the electrodes were computed from the discharge plot using Eq. (2) [79]

$$C_{sp} = \frac{I\Delta t}{m\Delta V} \quad (2)$$

where Δt is the discharge time (s). The outcomes demonstrate that the rGO@MVO electrode has higher capacitance than the other electrodes, as shown in Table 3. This can be attributed, as mentioned above, to the existence of the high conducting rGO in the composite electrode beside the synergistic effect produced from the constituent materials. The carbon atoms present in rGO allowed higher conductivity from carbon π-electron bonds. Also, the large quantity of oxygen with high electronegativity makes sure that the rGO is a highly conductive material. In conclusion, the existence of polar species in rGO and $Mn_2V_2O_7$

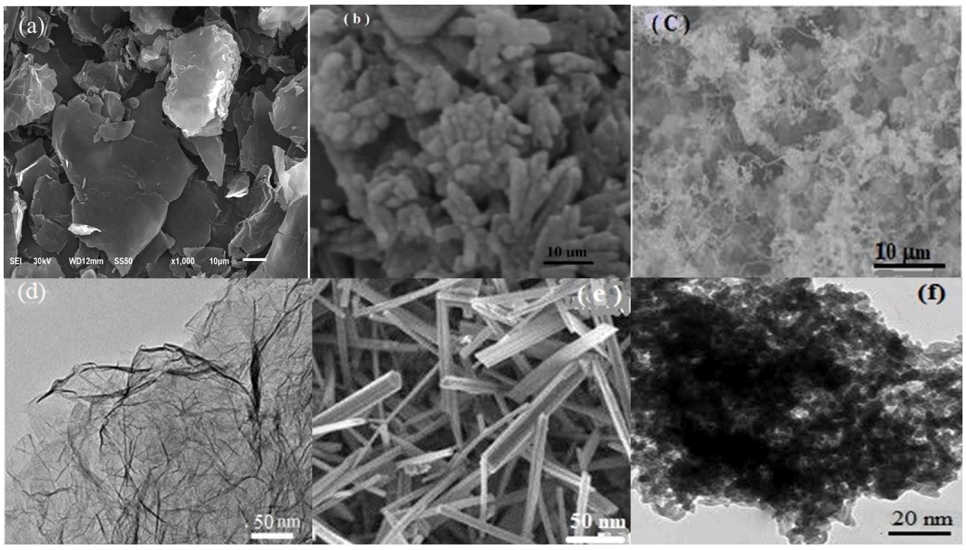


**Fig. 4.** SEM of rGO (a), $Mn_2V_2O_7$ (b), rGO@$Mn_2V_2O_7$ and TEM of rGO (d), $Mn_2V_2O_7$ (e), rGO@$Mn_2V_2O_7$ (f).

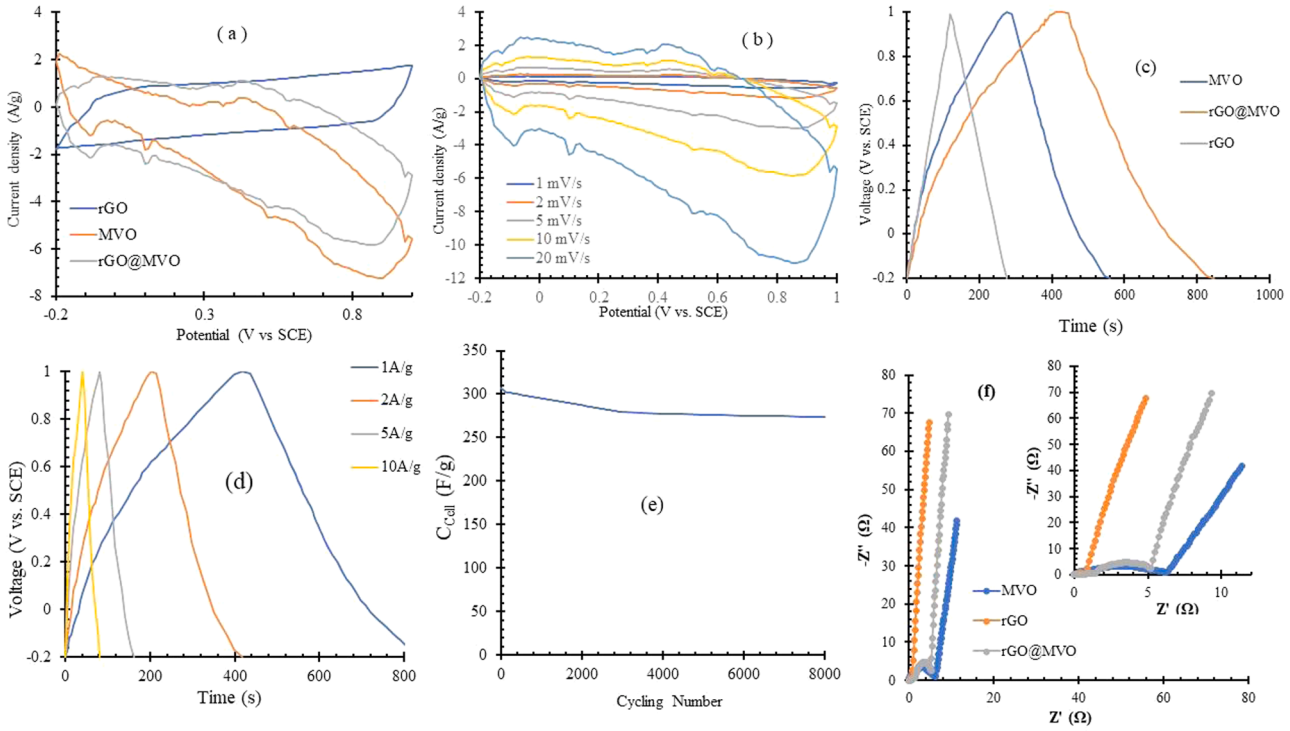


**Fig. 5.** CV of the investigated samples (a), CV of rGO@MVO at several scan rates (b), GCD plots of the investigated samples at 1 A/g (d), GCD plots of rGO@MVO at different current densities (d), stability of rGO@MVO electrode (e), and Nyquist plots of investigated samples (f).

**Table 3**
Specific capacitance of the investigated samples using CV and GCD techniques.

| samples | CV (F/g) | | | | GCD (F/g) | | | |
|---|---|---|---|---|---|---|---|---|
| | 1 mV/s | 5 mV/s | 10 mV/s | 20 mV/s | 1A/g | 2A/g | 5A/g | 10 A/g |
| rGO | 132 | 121 | 117 | 107 | 120 | 116 | 111 | 103 |
| MVO | 250 | 240 | 235 | 223 | 235 | 229 | 225 | 222 |
| rGO@MVO | 350 | 335 | 329 | 318 | 330 | 326 | 318 | 308 |

supported the materials inertly bonded by effective intermolecular dipole-dipole forces. As a result of these properties, improved specific capacitance and minimalized redox reactions were attained by rGO@$Mn_2V_2O_7$ nanocomposite.

The electrochemical performance of the rGO@MVO electrode, which has the highest capacitance of all the electrodes investigated, was studied at several current densities. The obtained outcomes are given in Fig. 5d and Table 3, illustrating a high capacitance at lower discharging current rates. This is attributed to that at the lower current densities, the inner active sites of the rGO@MVO electrode can be wholly employed owing to the low ohmic drop, which provides sufficient time for redox. On the other hand, at the high current densities, a predictable time

limitation for the redox process makes it difficult to provide high capacities [78,80].

The stability test for the rGO@MVO electrode was carried out up to 8000 cycles of GCD at a current density of 10 A $g^{-1}$. The result is illustrated in Fig. 5(e), which demonstrated 89% retention in the capacity after 8000 cycles. The long-term stability of the rGO@MVO electrode might be attached to the synergistic effects amongst the constituents of the binary system. This could be ascribed to that the rGO makes several mechanical deformations during the redox course of $Mn_2V_2O_7$ particles to become more stable by rGO, which organizes as a protecting layer; all of these collectively backing in developing the electrochemical stability.

### 3.5.1. Electrochemical impedance study of single electrodes

All the investigated electrodes were also analyzed by EIS at a frequency range between $10^{-2}$ and $10^{5}$ Hz. The acquired data were represented as Nyquist plots in Fig. 5f. The figure shows semicircles at higher frequencies. The intercept of the semicircle with $Z^{/}$-axis at the high-frequency region corresponds to the charge transfer resistance ($R_{CT}$) and solution resistance ($R_s$). At the same time, the almost straight line in the low-frequency range relates to the Warburg resistance ($W_D$). The MVO electrode demonstrates the largest semicircle, indicating its highly resistive property. In contrast, the small loops of rGO and rGO@MVO indicate their low electrical resistance. The ESR-value was determined from the first $Z^{/}$-intercept and slope of the Nyquist plot and found to be 0.51, 4.81, and 6.12 ohm for rGO, rGO@MVO, and MVO, respectively. The lower ESR value of the rGO@MVO compared to that of MVO is due to the covering of conducting rGO on the MVO surface. Fig. 5 f also shows that in the low-frequency region, rGO/MVO has more slope than the other electrodes, referring that the composite electrode has better capacitance than the others, which agrees with the CV results and GCD.

### 3.5.2. Asymmetric supercapacitor

The possibility of using the rGO@MVO electrode, with the highest capacity, in practical applications was ensured by fabricating an asymmetric supercapacitor cell consisting of rGO@MVO as a positive electrode, activated carbon as a negative electrode, and a LiTFSi-soaked PTFE electrolyte membrane. The capacitance of the AC- negative electrode was studied within a potential window of −1 to 0 V (versus SCE) at a scan rate of 10 mV/s, and the acquired outcomes are illustrated in Fig. 6a. The Figure shows a rectangular shape characterizing the electric double-layer capacitance. The $C_{sp}$ value of the AC electrode computed using Eq (2) is 190 F/g, which matches well with that found in the literature for commercial AC electrodes [81].

Grounded on the separate potential window of AC and rGO@MVO electrodes (Figs. 5a and 6a), the assembled ASC of rGO@MVO// AC can perform with an ideal capacitive characteristic at 2.0-V work voltage. For better performance ASC, the charge balance of the two electrodes should be equal, i.e., $q^{+} = q^{-}$. Accordingly, the mass balance between the positive and negative electrodes will follow Eq. (3) [47]

$$\frac{m^{-}}{m^{+}} = \frac{C_m^{+}}{C_m^{-}} \times \frac{V^{+}}{V^{-}} \tag{3}$$

Where $m$ is the mass of the electrode, c is the specific capacitance, $\Delta V$ is the potential window, and the superscripts "+" and "−" are the positive and negative electrodes, respectively. For the investigated ASC, the $\frac{m^{-}}{m^{+}} = 2.21$

Fig. 6b demonstrates the CV plots of the rGO@MVO//AC asymmetric supercapacitor at several scan rates. The CV shapes display the combination of the battery-type (rGO@MVO) and the EDLC-like (AC) materials validating the asymmetric nature. It was evident that all the curves have no noticeable change by changing the scan rate from 1 to 50 mV $s^{-1}$, manifesting the super electrochemical reversibility and rapid charge-discharge process.

The GCD of the ASC was also studied at several current densities between 1 and 10 A $g^{-1}$, and the results are demonstrated in 6c. The Figure shows that the charge and discharge portions of the GCD plots are nearly symmetry and exhibit a small internal resistance drop. The GCD plots were applied to calculate the corresponding specific capacity of the

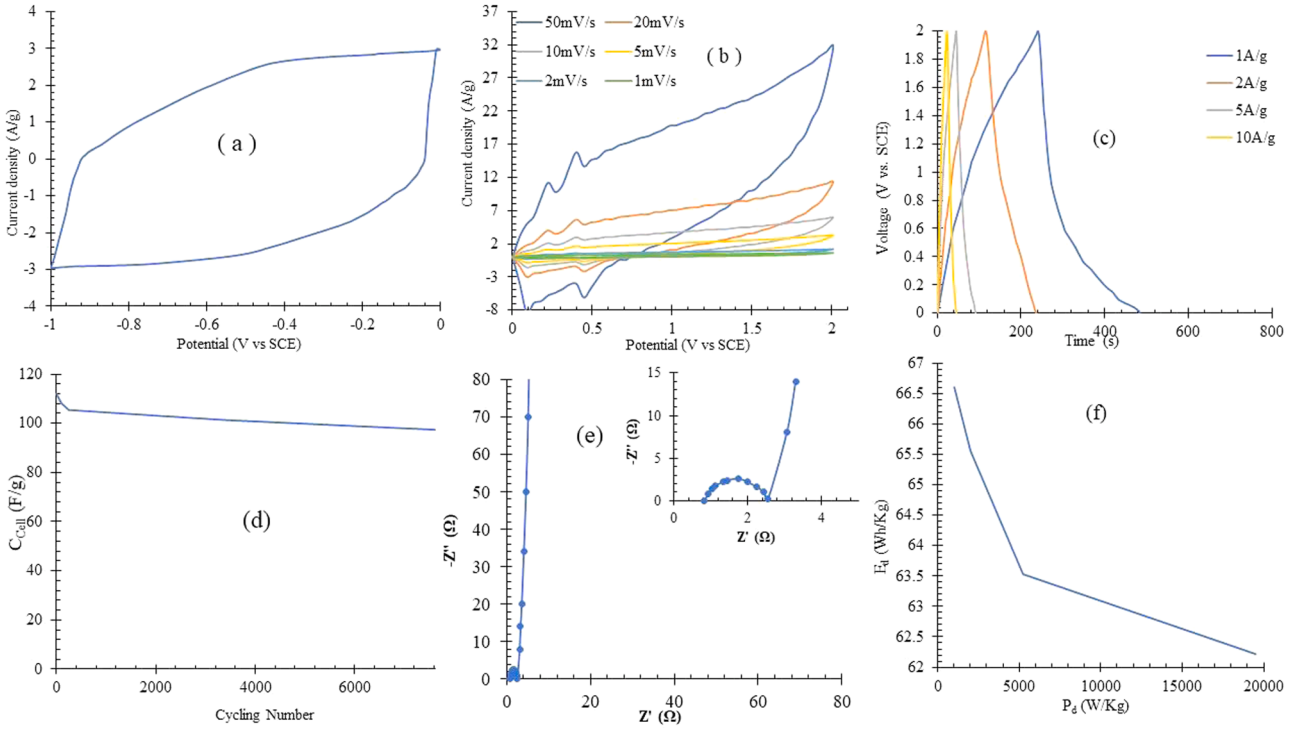


**Fig. 6.** Specific capacitance of rGO at 10 mV/s (a), Specific capacitance of rGO@MVO//AC asymmetric cell at several scan rates (b), GCD plot of rGO@MVO//AC asymmetric cell at different current densities (c), stability of rGO@MVO//AC asymmetric cell (d), Nyquist plot of rGO@MVO//AC asymmetric cell (e), and Ragone plot of the asymmetric cell (f).

ASC at different specific currents using Eq. (4) [82,83]

$$C_{cell} = \frac{I\Delta t}{M\Delta V} \quad (4)$$

where M is the whole mass of the active materials in both electrodes, and dV/dt is the slope of the discharge part. The specific capacitance calculated is 120, 118, 114, and 112 $Fg^{-1}$, respectively, at 1, 2, 5, and 10 $Ag^{-1}$. The capacitance of the ASC still retains 90.7% with a current density 10-fold increase, revealing a good capability rate. This can be attributed to the exceptional nanostructure properties with great surface area and high electrical conductivity of AC, which cause overflowing adsorption of ions besides an effective ion intercalation/deintercalation.

The cycling life of the ASC cell tested at a current density of 10 A $g^{-1}$ demonstrates high stability for the device, Fig. 6d. The cell only loses 13.4% of its initial capacitance value after 8000 cycles. The electrochemical behavior of the ASC was also studied using the EIS technique at a frequency ranging between $10^{-2}$ and $10^{5}$ Hz. The acquired data obtained are illustrated as a Nyquist plot in Fig. 6e. The Figure shows a depressed semicircle at higher frequencies followed by an almost straight line at lower frequencies, revealing a very low $R_s$-value of 0.83 Ω and the $R_{ct}$-value of only 1.60 Ω.

The energy density ($E_d$, Wh $kg^{-1}$) and power density ($P_d$, kW $kg^{-1}$) were usually used to evaluate the performance of ASCs. They can be assessed by Eqs. (4) and (5) [84]

$$E_d = C_{cell}(\Delta V)^2/7.2 \quad (4)$$

$$P_d = 3600E_d/\Delta t \quad (5)$$

All symbols are mentioned above. The data obtained at different current densities are represented as a Ragon plot in 6*f*, which showed the highest- value of 66.6 Wh/Kg and the highest $P_d$-value of 19478 W/kg. For comparison, Ragone data for other similar systems are listed in Table 4 [80–88].

### 3.6. Electro-catalyst for oxygen evolution reaction

The electro-catalytic activity of rGO@MVO and MVO electrodes for OER was studied using the conventional electrochemical linear sweep voltammetry (LSV) besides the above-mentioned electrochemical techniques in 1 M KOH solution. Fig 7a illustrates the LSV curves of the rGO@MVO electrode and MVO and CC for comparison. The results showed that the overpotentials at a current density of 10 mA/$cm^2$ for rGO@MVO, MVO, and CC are 225, 338, and 496 mV, respectively. Furthermore, the onset potentials obtained for the MVO and rGO@MVO are 1.465 V ~ and 1.435 V, respectively, lower than that of the traditional noble metal base electro-catalyst for OER ($IrO_2$, ~1.51 V), referring to their lower potential resistance for OER.

The Tafel slope values give a vision of the kinetics of the OER mechanism. The electrode with a lower Tafel slope has normal high-speed reaction kinetics that improves OER activity. The Tafel slopes of rGO@MVO, MVO, and CC were calculated from the corresponding Tafel plots, Fig. 7b. The rGO@MVO electrode exhibited a Tafel slope of 54 mV/dec, which is lower than the other electrodes: 57 mV/dec for MVO and 130 mV/dec for CC. All these outcomes approve that the rGO@MVO electrode has a better electro-catalytic activity for OER than other recently reported noble-metal-free OER catalysts such as A-$CoS_{4.6}O_{0.6}$ (290 mV) [37], $Fe_3O_4$@$Co_9S_8$ (320 mV) [94] $CoTe_2$ nanofleeces (357 mV) [95] $Co_3S_4$ nanosheets (363 mV) [96] and $Ni_2P$ (290 mV) [97], signifying the favorable electro-catalytic reaction kinetics of the rGO@MVO.

Electrochemical impedance spectroscopy (EIS) was recorded for rGO@MVO and MVO samples to further ratify the electrode kinetics. The data obtained are represented as Nyquist plots in Fig. 7(c). At the lower frequency region, the figure shows a semicircle for each one of the electro-catalysts, which is credited to the electron transfer resistance ($R_{ct}$) of the catalyst for OER. The semicircle diameter of rGO@MVO is (1.2 Ω) smaller than that of MVO (16.5 Ω), denoting a fast electron transfer of OER, i.e., faster OER kinetics; this might be attributed to the good connection between the GCE and the ultrathin nanofilms of rGO@MVO.

The stability of the investigated electrodes in 4 M KOH solution was examined using the chronopotentiometry technique at the constant current density of 10 $mAcm^{-2}$ for a period of 50 h. The results obtained are represented as potential versus time, Fig. 7d. The percentage change in the measured potential during 50 h is 1.5% for rGO@MVO, and 3.3% for MVO; referring to the stability of the investigated electrodes in the alkaline medium.

In general, the electrochemical active surface area (ECSA) is considered one of the determining factors behind the electrocatalytic activity of any material. The ECSA is proportional to the catalyst's electrochemical double-layer capacitance ($C_{dl}$) [21]. The $C_{dl}$ of the investigated catalyst was fixed by measuring the CV in the non-Faradaic region at scan rates between 10 and 100 mV/s, Fig. 7 e,f. The $C_{dl}$ value of rGO@MVO is 12.8 mF $cm^{-2}$ higher than that of 11.7 mF $cm^{-2}$ found for MVO. The excellent overall water splitting performance of the rGO@MVO electro-catalyst could be attributed to its structure with high surface area and the sufficient contact between the electrode and electrolyte to facilitate the electrolyte diffusion and ionic transport.

**Table 4**
A comparison between electrochemical data of some asymmetric supercapacitors configuration found in literature and the data of the present work.

| Material | $E_d$ (Wh/kg) | $P_d$ (W/kg) | Ref. |
|---|---|---|---|
| $MnCo_2O_4$ //AC | 10.04 | 5000.2 | [85] |
| $NiCoFe_2O_4$//AC | 4.79 | 1426.23 | [86] |
| $NiCuFe_2O_4$//AC | 4.62 | 1001.29 | [86] |
| $ZnCo_2O_4$//$FeCo_2O_4$ | 25.45 | 3620 | [87] |
| $CuCoFe_2O_4$ //AC | 7.9 | 1711.95 | [86] |
| $NiMoO_4$//AC | 48.5 | 212.5 | [88] |
| $Co_3O_4$ -NiO/GO//AC | 50.2 | 825 | [89] |
| $MnCo_2O_{4.5}$-40GQDs//rGO | 46 | 66 | [90] |
| $CoMoO_4$@CoS//AC | 59.5 | 799.8 | [91] |
| $CuCo_2S_4$//NG | 32.7 | 794 | [92] |
| α-$LiFe_5O_8$//NiO | 30 | 794 | [93] |
| rGO@$Mn_2V_2O_7$//AC | 66.6 | 19478 | This work |

## 4. Conclusions

Manganese vanadate (MVO) and rGO have been synthesized for supercapacitors and electrocatalytic applications. The single electrodes of the investigated samples showed a specific capacitance of 120, 235, and 330 F/g for rGO, MVO, and rGO@MVO, respectively, in an electrolyte of 1M of $LiClO_4$ in propylene carbonate solution. An asymmetric supercapacitor (ASC) of rGO@MVO composite as a positive electrode and activated carbon (AC) as a negative electrode delivers a high energy density of 66.6 Wh $kg^{-1}$ at a power density of 19478 W $kg^{-1}$. It has reasonable cycle stability with 89% capacitance retention over 8000 cycles. The MVO and rGO@$Mn_2V_2O_7$ catalyst hold an overpotential of 225 and 338 mV, respectively, for oxygen evolution reaction at 10 mA $cm^{-2}$.

## CRediT authorship contribution statement

**E.A. Kamar:** Funding acquisition, Investigation, Resources, Validation, Writing – original draft, Writing – review & editing. **K.F. Qasim:** Data curation, Formal analysis, Methodology, Software, Writing – original draft, Writing – review & editing. **M.A. Mousa:** Conceptualization, Project administration, Supervision, Visualization, Writing – original draft, Writing – review & editing.

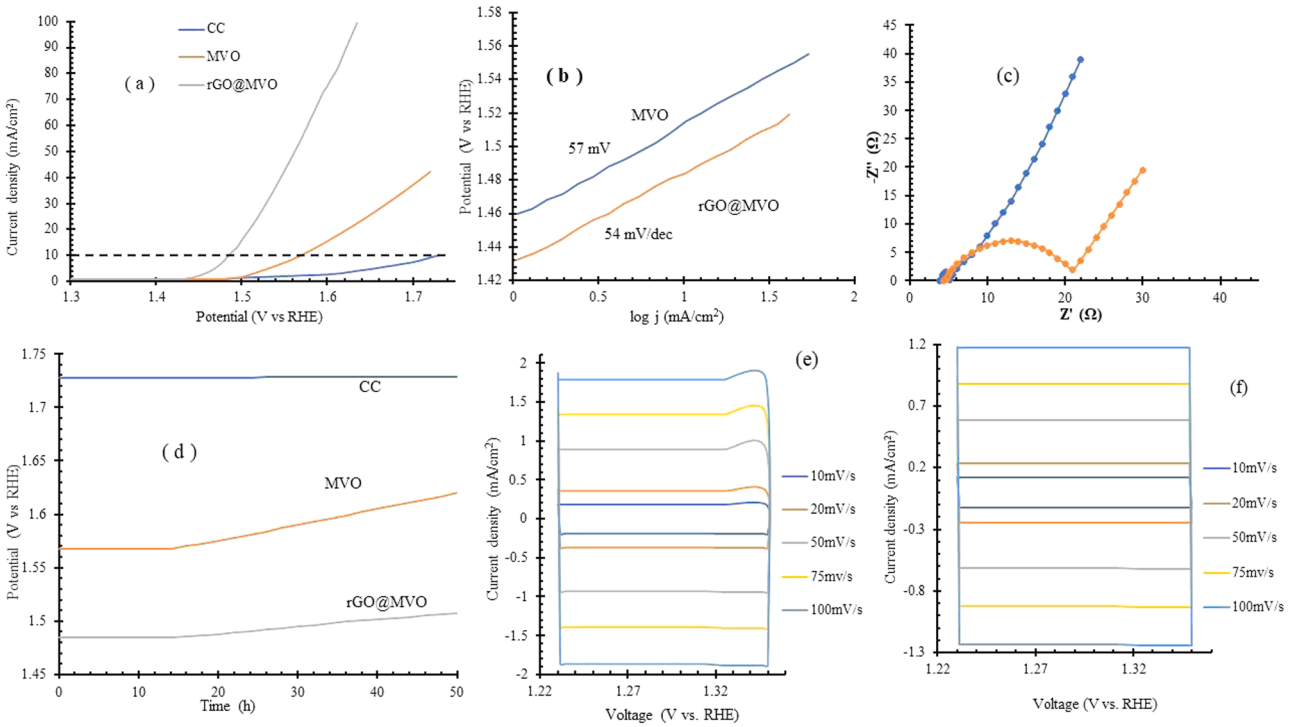


**Fig. 7.** Electrochemical performance and electrochemical double-layer capacitance (Cdl) of CC, MVO, and rGO@ MVO for OER activity in 1 M KOH solution: (a) Linear sweep voltammetry, (b) Tafel plots, (c) Nyquist plots, (d) stability of the electrode, (e) $C_{dl}$ of rGO@MVO and (f) $C_{dl}$ of MVO.

## Declaration of Competing Interest

The authors declare no competing interests.

## Data Availability

Data will be made available on request.

## References


[1] D. Yan, Y. Li, J. Huo, R. Chen, L. Dai, S. Wang, Defect chemistry of nonprecious-metal electrocatalysts for oxygen reactions, Adv. Mater. 1606459 (2017) 1–20, https://doi.org/10.1002/adma.201606459.

[2] D. Zhao, H. Liu, X. Wu, Bi-interface induced multi-active $MCo_2O_4$@$MCo_2S_4$@PPy (M=Ni, Zn) sandwich structure for energy storage and electrocatalysis, Nano Energy 57 (2018) 363–370, https://doi.org/10.1016/j.nanoen.2018.12.066.

[3] C. Liu, X. Wu, B. Wang, Performance modulation of energy storage devices : a case of Ni-Co-S electrode materials, Chem. Eng. J. (2019), 123651, https://doi.org/10.1016/j.cej.2019.123651.

[4] B. Ni, L. Wu, R. Chen, C. Shi, T. Chen, Fe/Co-based nanoparticles encapsulated in heteroatom-doped carbon electrocatalysts for oxygen reduction reaction, Sci. China Mater. 62 (2019) 1–16.

[5] H. Liu, D. Zhao, P. Hu, K. Chen, X. Wu, D. Xue, Design strategies toward achieving high-performance $CoMoO_4$@ $Co_{1.62}Mo_6S_8$ electrode materials, Mater. Today Phys. 13 (2020), 100197, https://doi.org/10.1016/j.mtphys.2020.100197.

[6] Y. Huang, M. Li, W. Yang, Y. Yu, S. Hao, 3D ordered mesoporous cobalt ferrite phosphides for overall water splitting, Sci. China Mater. 63 (2019) 240–248.

[7] J.P. Barton, D.G. Infield, Energy storage and its use with intermittent renewable energy, IEEE Trans. Energy Convers. 19 (2004) 441–448.

[8] Y. Xu, H. Ming, Electrocatalysis for the oxygen evolution reaction: recent development and future perspectives, Chem. Soc. Rev. 46 (2017) 337–365, https://doi.org/10.1039/c6cs00328a.

[9] Y. Shi, B. Zhang, Recent advances in transition metal phosphide nanomaterials: synthesis and applications in, Chem. Soc. Rev. 45 (2016) 1529–1541, https://doi.org/10.1039/C5CS00434A.

[10] C. Zhao, Y. Huang, C. Zhao, X. Shao, Z. Zhu, Rose-derived 3D carbon nanosheets for high cyclability and extended voltage supercapacitors, Electrochim. Acta. 291 (2018) 287–296, https://doi.org/10.1016/j.electacta.2018.09.136.

[11] K. Krishnamoorthy, S. Thangavel, J. Chelora, N. Raju, Graphdiyne nanostructures as a new electrode material for electrochemical supercapacitors, Int. J. Hydrogen Energy. 41 (2015) 1–7, https://doi.org/10.1016/j.ijhydene.2015.10.118.

[12] S. Zhu, W. Wang, Y. Xu, Z. Zhu, Z. Liu, F. Cui, Iron sludge-derived magnetic $Fe^0$/$Fe_3C$ catalyst for oxidation of ciprofloxacin via peroxymonosulfate activation, Chem. Eng. J. 365 (2019) 99–110, https://doi.org/10.1016/j.cej.2019.02.011.

[13] Y. Zhou, Z. Zhu, C. Zhao, K. Zhang, B. Wang, C. Zhao, G. Chen, Reclaimed carbon fiber-based 2.4 V aqueous symmetric supercapacitors, ACS Sustain. Chem. Eng. 7 (2019) 2–9, https://doi.org/10.1021/acssuschemeng.8b05951.

[14] Y. Liang, Q. Liu, Y. Luo, X. Sun, Y. He, A.M. Asiri, $Zn_{0.76}Co_{0.24}S/CoS_2$ nanowires array for efficient electrochemical splitting of water, Electrochim. Acta. 190 (2016) 360–364, https://doi.org/10.1016/j.electacta.2015.12.153.

[15] V.A. Yartys, et al., Magnesium based materials for hydrogen based energy storage: past, present and future, Int. J. Hydrogen Energy. 44 (2019) 7809–7859, https://doi.org/10.1016/j.ijhydene.2018.12.212.

[16] Y. Dong, J. Yang, Y. Liu, Y. Wang, Z. Dong, M. Cui, M. Li, X. Yuan, X. Zhang, X. Dai, 2D Fe-doped NiO nanosheets with grain boundary defects for the advanced oxygen evolution reaction, Dalt. Trans. 49 (2020) 6355–6362, https://doi.org/10.1039/c9dt04633j.

[17] J. Feng, H. Xu, Y. Dong, S. Ye, Y. Tong, G. Li, FeOOH/Co/FeOOH hybrid nanotube arrays as high-performance electrocatalysts for the oxygen evolution reaction, Angew. Chemie - Int. Ed. 55 (2016) 3694–3698, https://doi.org/10.1002/anie.201511447.

[18] Y. Tian, Z. Zhang, Y. Miao, Co-Te-Se nano-compounds as electrocatalysts for hydrogen evolution reaction, J. Electrochem. Soc. 163 (2016) 625–629, https://doi.org/10.1149/2.0251608jes.

[19] M. Xiao, Z. Zhang, Y. Tian, Y. Miao, Co–Fe–Se ultrathin nanosheet-fabricated microspheres for efficient electrocatalysis of hydrogen evolution, J. Appl. Electrochem. 47 (2016) 361–367, https://doi.org/10.1007/s10800-016-1014-5.

[20] J. Zhang, Q. Zhang, X. Feng, Support and interface effects in water-splitting electrocatalysts, Adv. Mater. 31 (2019) 1–19, https://doi.org/10.1002/adma.201808167.

[21] I.K. Mishra, H. Zhou, J. Sun, K. Dahal, Z. Ren, R. He, S. Chen, Z. Ren, Highly efficient hydrogen evolution by self-standing nickel phosphide-based hybrid nanosheet arrays electrocatalyst, Mater. Today Phys. 4 (2018) 1–6, https://doi.org/10.1016/j.mtphys.2018.01.001.

[22] X. Li, X. Hao, A. Abudula, G. Guan, Nanostructured catalysts for electrochemical water splitting: current state and prospects, J. Mater. Chem. A. 4 (2016) 11973–12000, https://doi.org/10.1039/C6TA02334G.

[23] J. Wang, W. Cui, Q. Liu, Z. Xing, A.M. Asiri, X. Sun, Recent progress in cobalt-based heterogeneous catalysts for electrochemical water splitting, Adv. Mater. 28 (2016) 215–230, https://doi.org/10.1002/adma.201502696.

[24] Z.W. Seh, J. Kibsgaard, C.F. Dickens, I. Chorkendorff, J.K. Nørskov, T.F. Jaramillo, Combining theory and experiment in electrocatalysis: insights into materials design, Science (80-.) 355 (2017) 146, https://doi.org/10.1126/science.aad4998.

[25] X. Xiao, D. Huang, Y. Qing, R. Fu, M. Wen, X. Jiang, Engineering NiS/Ni2P heterostructures for efficient electrocatalytic water splitting, ACS Appl. Mater. Interfaces 10 (2018) 4689–4696, https://doi.org/10.1021/acsami.7b16430.

[26] V. Vij, S. Sultan, A.M. Harzandi, A. Meena, N. Tiwari, W.G. Lee, T. Yoon, K.S. Kim, Nickel – based electrocatalysts for energy related applications : oxygen reduction,

oxygen evolution, and hydrogen evolution reactions, ACS Catal. 7 (2017) 7196–7225, https://doi.org/10.1021/acscatal.7b01800.
[27] L. Lv, Z. Yang, K. Chen, C. Wang, Y. Xiong, 2D layered double hydroxides for oxygen evolution reaction: from fundamental design to application, Adv. Energy Mater. 1803358 (2019) 1–29, https://doi.org/10.1002/aenm.201803358.
[28] C.C.L. Mccrory, S. Jung, J.C. Peters, T.F. Jaramillo, Benchmarking heterogeneous electrocatalysts for the oxygen evolution reaction, J. Am. Chem. Soc. 135 (2013) 16977–16987, https://doi.org/10.1021/ja407115p.
[29] M.G. Walter, E.L. Warren, J.R. Mckone, S.W. Boettcher, Q. Mi, E.A. Santori, N. S. Lewis, Solar water splitting cells, Chem. Rev. 110 (2010) 6446–6473, https://doi.org/10.1021/cr1002326.
[30] Q. Gao, W. Zhang, Z. Shi, L. Yang, Y. Tang, Structural design and electronic modulation of transition- metal-carbide electrocatalysts toward efficient hydrogen evolution, Adv. Mater. 1802880 (2018) 1–35, https://doi.org/10.1002/adma.201802880.
[31] T. Zhan, X. Liu, S. Lu, W. Hou, Nitrogen doped NiFe layered double hydroxide/reduced graphene oxide mesoporous nanosphere as effective bifunctional electrocatalyst for oxygen reduction and evolution reactions, Appl. Catal. B Environ. 205 (2017) 551–558, https://doi.org/10.1016/j.apcatb.2017.01.010.
[32] J. Vazquez-samperio, M.A. Oliver-tolentino, A. Guzma, N. Nava, N. Castillo, M. J. Maci, Materials influence of cobalt on electrocatalytic water splitting in NiCoFe layered double hydroxides, J. Mater. Sci. 53 (2018) 4515–4526, https://doi.org/10.1007/s10853-017-1882-z.
[33] M. Al-mamun, X. Su, H. Zhang, H. Yin, P. Liu, H. Yang, D. Wang, Z. Tang, Y. Wang, H. Zhao, Strongly coupled $CoCr_2O_4$/carbon nanosheets as high performance electrocatalysts for oxygen evolution reaction, Small 12 (2016) 2866–2871, https://doi.org/10.1002/smll.201600549.
[34] S. Hirai, S. Yagi, A. Seno, M. Fujioka, Enhancement of the oxygen evolution reaction in Mn3+-based electrocatalysts: correlation between Jahn–Teller distortion and catalytic activity, RSC Adv. 6 (2016) 2019–2023, https://doi.org/10.1039/c5ra22873e.
[35] A.T. Swesi, J. Masud, M. Nath, Nickel selenide as a high-efficiency catalyst for oxygen evolution reaction, Energy Environ. Sci. 9 (2016) 1771–1782, https://doi.org/10.1039/c5ee02463c.
[36] X. Xu, F. Song, X. Hu, A nickel iron diselenide-derived efficient oxygen-evolution catalyst, Nat. Commun. 7 (2016) 12324, https://doi.org/10.1038/ncomms12324.
[37] P. Cai, J. Huang, J. Chen, Z. Wen, Oxygen-incorporated amorphous cobalt sulfide porous nanocubes as high-activity electrocatalysts for the oxygen evolution reaction in an alkaline/neutral medium, Angew. Chemie - Int. Ed. 56 (2017) 1–5, https://doi.org/10.1002/anie.201701280.
[38] B. Dong, X. Zhao, G. Han, X. Li, X. Shang, Y. Liu, Two-step synthesis of binary Ni–Fe sulfides supported on nickel foam as highly efficient electrocatalysts for the oxygen evolution reaction †, J. Mater. Chem. A 4 (2016) 13499–13508, https://doi.org/10.1039/c6ta03177c.
[39] Y. Zhang, B. Ouyang, J. Xu, G. Jia, S. Chen, R.S. Rawat, H.J. Fan, Electrocatalysis very important paper rapid synthesis of cobalt nitride nanowires: highly efficient and low-cost catalysts for oxygen evolution, Angew. Chemie - Int. Ed. 55 (2016) 1–6, https://doi.org/10.1002/anie.201604372.
[40] P. Chen, K. Xu, Y. Tong, X. Li, S. Tao, Z. Fang, W. Chu, X. Wu, C. Wu, Cobalt nitrides as a class of metallic electrocatalysts for the oxygen evolution reaction, Inorg. Chem. Front. 3 (2016) 236, https://doi.org/10.1039/c5qi00197h.
[41] L. Cui, F. Qu, J. Liu, G. Du, A.M. Asiri, X. Sun, Interconnected network of shell-core Co-Bi-Pi @ CoP for efficient water oxidation electrocatalysis under near neutral conditions, ChemSusChem (2017) 10, https://doi.org/10.1002/cssc.201700113.
[42] J. Masa, I. Sinev, H. Mistry, E. Ventosa, M. De Mata, J. Arbiol, M. Muhler, B. R. Cuenya, W. Schuhmann, Ultrathin high surface area nickel boride ($Ni_xB$) nanosheets as highly efficient electrocatalyst for oxygen evolution, Adv. Energy Mater. 7 (2017) 1–8, https://doi.org/10.1002/aenm.201700381.
[43] H. Wang, Y. Cao, C. Sun, G. Zou, J. Huang, X. Kuai, Strongly coupled molybdenum carbide @ carbon sheets as a bifunctional electrocatalyst for overall water splitting, ChemSusChem 10 (2017) 3540–3546, https://doi.org/10.1002/cssc.201701276.
[44] J. Jiang, Q. Liu, C. Zeng, L. Ai, Cobalt/molybdenum carbide @N-doped carbon as a bifunctional electrocatalyst for hydrogen and oxygen evolution reactions, J. Mater. Chem. A 5 (2017) 16929–16935, https://doi.org/10.1039/c7ta04893a.
[45] B. Wurster, D. Grumelli, D. Hötger, R. Gutzler, K. Kern, B. Wurster, D. Grumelli, D. Hötger, R. Gutzler, K. Kern, Driving the oxygen evolution reaction by nonlinear cooperativity in bimetallic coordination catalysts, J. Am. Chem. Soc. 138 (2016) 3623–3626, https://doi.org/10.1021/jacs.5b10484.
[46] S.W. Sheehan, J.M. Thomsen, U. Hintermair, R.H. Crabtree, G.W. Brudvig, C. A. Schmuttenmaer, A molecular catalyst for water oxidation that binds to metal oxide surfaces, Nat. Commun. 6 (2015) 6469–6475, https://doi.org/10.1038/ncomms7469.
[47] M. Khairy, W.A. Bayoumy, K.F. Qasim, E. El-Shereafy, M.A. Mousa, Ternary V-doped $Li_4Ti_5O_{12}$-polyaniline-graphene nanostructure with enhanced electrochemical capacitance performance, Mater. Sci. Eng. B 271 (2021), 115312, https://doi.org/10.1016/j.mseb.2021.115312.
[48] B. Chameh, M. Moradi, S. Hajati, F.A. Hessari, Design and construction of ZIF (8 and 67) supported $Fe_3O_4$ composite as advanced materials of high performance supercapacitor, Phys. E Low-dimensional Syst. Nanostruct. 126 (2021), 114442, https://doi.org/10.1016/j.physe.2020.114442.
[49] W. Niu, Z. Xiao, S. Wang, S. Zhai, L. Qin, Z. Zhao, Synthesis of nickel sulfide-supported on porous carbon from a natural seaweed-derived polysaccharide for high-performance supercapacitors, J. Alloys Compd. 853 (2021), 157123, https://doi.org/10.1016/j.jallcom.2020.157123.
[50] T. Pettong, P. Iamprasertkun, A. Krittayavathananon, P. Sukhaa, P. Sirisinudomkit, A. Seubsai, M. Chareonpanich, P. Kongkachuichay, J. Limtrakulc, M. Sawangphruk, High-performance asymmetric supercapacitors of $MnCo_2O_4$ nanofibers and N-doped reduced graphene oxide aerogel, ACS Appl. Mater. Interfaces 8 (2016) 34045–34053, https://doi.org/10.1021/acsami.6b09440.
[51] L. Sun, Q. Fu, C. Pan, Mn3O4 embedded 3D multi-heteroatom co-doped carbon sheets /carbon foams composites for high-performance flexible supercapacitors, J. Alloys Compd. 849 (2020), 156666, https://doi.org/10.1016/j.jallcom.2020.156666.
[52] K.F. Qasim, W.A. Bayoumy, M.A. Mousa, Electrical and electrochemical studies of core–shell structured nanorods of $LiMn_2O_4$@PANI composite, J. Mater. Sci. Mater. Electron. 31 (2020) 19526–19540, https://doi.org/10.1007/s10854-020-04482-5.
[53] M. Zhang, Z. Song, H. Liu, A. Wang, S. Shao, $MoO_2$ coated few layers of $MoS_2$ and $FeS_2$ nanoflower decorated S-doped graphene interoverlapped network for high-energy asymmetric supercapacitor, J. Colloid Interface Sci. 584 (2021) 418–428, https://doi.org/10.1016/j.jcis.2020.10.005.
[54] V. Augustyn, B. Dunn, Pseudocapacitive oxide materials for high-rate electrochemical energy storage, Energy Environ. Sci. 7 (2014) 1597–1614, https://doi.org/10.1039/c3ee44164d.
[55] P. Wu, S. Cheng, M. Yao, L. Yang, Y. Zhu, P. Liu, A Low-Cost, Self-standing $NiCo_2O_4$@CNT/CNT multilayer electrode for flexible asymmetric solid-state supercapacitors, Adv. Funct. Mater. 27 (2017) 1–9, https://doi.org/10.1002/adfm.201702160.
[56] Y. Liu, G. Huang, Y. Li, Y. Yao, Q. Liu, B. Xing, Structural evolution of porous graphitic carbon nanosheets based on quinonyl decomposition for supercapacitor electrodes, Appl. Surf. Sci. 537 (2021), 147824, https://doi.org/10.1016/j.apsusc.2020.147824.
[57] B. Anasori, M.R. Lukatskaya, Y. Gogotsi, 2D metal carbides and nitrides (MXenes) for energy storage, Nat. Rev. 2 (2017) 16098, https://doi.org/10.1038/natrevmats.2016.98.
[58] M. Zang, N. Xu, G. Cao, Z. Chen, J. Cui, Cobalt molybdenum oxide-derived high-performance electrocatalyst for hydrogen evolution reaction, ACS Catal. 8 (2018) 5062–5069, https://doi.org/10.1021/acscatal.8b00949.
[59] L. Liardet, X. Hu, Amorphous cobalt vanadium oxide as a highly active electrocatalyst for oxygen evolution, ACS Catal. 8 (2018) 644–650, https://doi.org/10.1021/acscatal.7b03198.
[60] S.H. Ryu, A.M. Shanmugharaj, W.S. Choi, Thermally reduced graphene oxide-supported nickel catalyst for hydrogen production by propane steam reforming, Appl. Catal. A Gen. 468 (2013) 467–474, https://doi.org/10.1016/j.apcata.2013.09.025.
[61] J. Biemolt, K. Zhao, Y. Zhao, G. Rothenberg, N. Yan, A membrane-free flow electrolyzer operating at high current density using earth-abundant catalysts for water splitting, Nat. Commun. 21 (2021) 4143, https://doi.org/10.1038/s41467-021-24284-5.
[62] M. Khairy, K. Faisal, M.A. Mousa, High-performance hybrid supercapacitor based on pure and doped $Li_4Ti_5O_{12}$ and graphene, J. Solid State Electrochem. 21 (2017) 873–882, https://doi.org/10.1007/s10008-016-3433-y.
[63] O. Namsar, T. Autthawong, R. Boonprachai, A. Yu, T. Sarakonsri, Enhancement in lithium storage performances of $SiO_2$/graphene-based nanocomposites prepared by low cost and facile approach, J. Mater. Sci. Mater. Electron. 33 (2022) 6536–6548, https://doi.org/10.1007/s10854-022-07828-3.
[64] A. Ram, P. Hillebrand, D. Stellmach, M.M. May, P. Bogdano, S. Fiechter, Evaluation of $MnO_x$, $Mn_2O_3$, and $Mn_3O_4$ electrodeposited films for the oxygen evolution reaction of water, J. Phys. Chem. C. 118 (2014) 14073–14081.
[65] A.M. Ezhil, S.G. Victoria, V.B. Jothy, C. Ravidhas, J. Wollschla, M. Suendorf, M. Neumann, M. Jayachandran, C. Sanjeeviraja, XRD and XPS characterization of mixed valence $Mn_3O_4$ hausmannite thin films prepared by chemical spray pyrolysis technique, Appl. Surf. Sci. 256 (2010) 2920–2926, https://doi.org/10.1016/j.apsusc.2009.11.051.
[66] G. Silversmit, D. Depla, H. Poelman, G.B. Marin, R. De Gryse, An XPS study on the surface reduction of $V_2O_5$ (001) induced by Ar+ ion bombardment, Surf. Sci. 600 (2006) 3512–3517, https://doi.org/10.1016/j.susc.2006.07.006.
[67] G. Silversmit, D. Depla, H. Poelman, G.B. Marin, R. De Gryse, Determination of the V2p XPS binding energies for different vanadium oxidation states ($V^{5+}$ to $V^{0+}$), J. Electron Spectros. Relat. Phenomena. 135 (2004) 167–175, https://doi.org/10.1016/j.elspec.2004.03.004.
[68] J. Mendialdua, R. Casanova, Y. Barbaux, XPS studies of $V_2O_5$, $V_6O_{13}$, $VO_2$ and $V_2O_3$, J. Electron Spectros. Relat. Phenomena. 71 (1995) 249–261.
[69] S. Grebinskij, V. Bondarenka, B. Vengalis, K. Sliu, Investigation of epitaxial $LaNiO_{3-x}$ thin films by high-energy XPS, J. Alloys Compd. 423 (2006) 107–111, https://doi.org/10.1016/j.jallcom.2005.12.038.
[70] Z. Zhou, Y. Zhang, Z. Wang, W. Wei, W. Tang, J. Shi, R. Xiong, Applied surface science electronic structure studies of the spinel $CoFe_2O_4$ by X-ray photoelectron spectroscopy, Appl. Surf. Sci. 254 (2008) 6972–6975, https://doi.org/10.1016/j.apsusc.2008.05.067.
[71] G. Ren, J. Lan, K.J. Ventura, X. Tan, Y. Lin, C. Nan, Contribution of point defects and nano-grains to thermal transport behaviours of oxide-based thermoelectrics, Nat. Publ. (2016) 1–9, https://doi.org/10.1038/npjcompumats.2016.23.
[72] Y.H. Tan, J.A. Davis, K. Fujikawa, N.V. Ganesh, V. Demchenko, K.J. Stine, Surface area and pore size characteristics of nanoporous gold subjected to thermal, mechanical, or surface modification studied using gas adsorption, J. Mater. Chem. 22 (2012) 6733–6745, https://doi.org/10.1039/c2jm16633j.
[73] M. Khairy, W.A. Bayoumy, K. Faisal, E.E. Elshereafy, M.A. Mousa, Electrical and electrochemical behavior of binary $Li_4Ti_5O_{12}$–polyaniline composite, J. Inorg. Organomet. Polym. Mater. 30 (2020) 3158–3169, https://doi.org/10.1007/s10904-020-01478-w.

[74] R. Farma, M. Deraman, I.A. Talib, R. Omar, J.G. Manjunatha, M.M. Ishak, Physical and electrochemical properties of supercapacitor electrodes derived from carbon nanotube and biomass carbon, Int. J. Electrochem. Sci. 8 (2013) 257–273.
[75] H. Li, J. Wang, Q. Chu, Z. Wang, F. Zhang, S. Wang, Theoretical and experimental specific capacitance of polyaniline in sulfuric acid, J. Power Sources. 190 (2009) 578–586, https://doi.org/10.1016/j.jpowsour.2009.01.052.
[76] R.K. Selvan, I. Perelshtein, N. Perkas, A. Gedanken, Synthesis of hexagonal-shaped $SnO_2$ nanocrystals and $SnO_2$@C nanocomposites for electrochemical redox supercapacitors, J. Phys. Chem. C 112 (2008) 1825–1830.
[77] K.F. Qasim, M.A. Mousa, Electrical and dielectric properties of self-assembled polyaniline on barium sulphate surface, Egypt. J. Pet. 30 (2021) 9–19, https://doi.org/10.1016/j.ejpe.2021.09.001.
[78] T. Qi, J. Jiang, H. Chen, H. Wan, L. Miao, L. Zhang, Effect of $Fe_3O_4$/reduced graphene oxide nanocomposites for supercapacitors with good cycling life, Electrochim. Acta. 114 (2013) 674–680, https://doi.org/10.1016/j.electacta.2013.10.068.
[79] K.F. Qasim, M.A. Mousa, Effect of oxidizer on PANI for producing $BaTiO_3$@PANI perovskite composites and their electrical and electrochemical properties, J. Inorg. Organomet. Polym. Mater. (2022), https://doi.org/10.1007/s10904-022-02335-8.
[80] H. Farsi, F. Gobal, Z. Barzgari, A study of hydrated nanostructured tungsten trioxide as an electroactive material for pseudocapacitors, Ionics (Kiel) 19 (2013) 287–294, https://doi.org/10.1007/s11581-012-0726-8.
[81] P. Gao, A. Lu, W. Li, Dual functions of activated carbon in a positive electrode for $MnO_2$ -based hybrid supercapacitor, J. Power Sources. 196 (2011) 4095–4101, https://doi.org/10.1016/j.jpowsour.2010.12.056.
[82] M. Sun, J. Tie, G. Cheng, T. Lin, S. Peng, F. Deng, F. Ye, In situ growth of burl-like nickel cobalt sulfide on carbon fibers as high-performance supercapacitors, J. Mater. Chem. A. 3 (2015) 1730–1736, https://doi.org/10.1039/c4ta04833d.
[83] K. Huang, L. Wang, Y. Liu, Y. Liu, H. Wang, T. Gan, L. Wang, Layered MoS2-graphene composites for supercapacitor applications with enhanced capacitive performance, Int. J. Hydrogen Energy. 38 (2013) 14027–14034, https://doi.org/10.1016/j.ijhydene.2013.08.112.
[84] M.A. Mousa, M. Khairy, M. Shehab, Nanostructured ferrite/graphene/polyaniline using for supercapacitor to enhance the capacitive behavior, J. Solid State Electrochem. 21 (2017) 995–1005, https://doi.org/10.1007/s10008-016-3446-6.
[85] S. Sahoo, K.K. Naik, C.S. Rout, Electrodeposition of spinel $MnCo_2O_4$ nanosheets for supercapacitor applications, Nanotechnology 26 (2015), 455401, https://doi.org/10.1088/0957-4484/26/45/455401.
[86] B. Bhujun, M.T. Tan, A.S. Shanmugam, Study of mixed ternary transition metal ferrites as potential electrodes for supercapacitor applications, Results Phys. (2016), https://doi.org/10.1016/j.rinp.2016.04.010.
[87] G.P. Kamble, A.A. Kashale, S.S. Kolekar, I.P. Chen, B.R. Sathe, Reflux temperature-dependent zinc cobaltite nanostructures for asymmetric supercapacitors, J. Mater. Sci. Mater. Electron. 32 (2021) 5859–5869, https://doi.org/10.1007/s10854-021-05306-w.
[88] X. Zhang, Z. Li, Z. Yu, L. Wei, X. Guo, Mesoporous $NiMoO_4$ microspheres decorated by Ag quantum dots as cathode material for asymmetric supercapacitors: enhanced interfacial conductivity and capacitive storage, Appl. Surf. Sci. 505 (2019), 144513, https://doi.org/10.1016/j.apsusc.2019.144513.
[89] X. Yang, C. Xiang, Y. Zou, J. Liang, H. Zhang, E. Yan, Low-temperature synthesis of sea urchin-like Co-Ni oxide on graphene oxide for supercapacitor electrodes, J. Mater. Sci. Technol. 55 (2020) 223–230, https://doi.org/10.1016/j.jmst.2020.03.026.
[90] M. Zhang, W. Liu, R. Liang, R. Tjandra, A. Yu, Graphene quantum dot induced tunable growth of nanostructured MnCo2O4.5 composites for high-performance supercapacitors, Sustain. Energy Fuels. 3 (2019) 2499–2508, https://doi.org/10.1039/c9se00341j.
[91] H. Xuan, H. Li, J. Yang, X. Liang, Z. Xie, P. Han, Y. Wu, Rational design of hierarchical core-shell structured $CoMoO_4$@CoS composites on reduced graphene oxide for supercapacitors with enhanced electrochemical performance, Int. J. Hydrogen Energy. 45 (2020) 6024–6035, https://doi.org/10.1016/j.ijhydene.2019.12.178.
[92] H. Dong, Y. Li, H. Chai, Y. Cao, X. Chen, Hydrothermal Synthesis of $CuCo_2S_4$ Nanostructure and N-Doped Graphene for High-Performance Aqueous Asymmetric Supercapacitors, ES Energy Environ 4 (2019) 19–26, https://doi.org/10.30919/esee8c221.
[93] J.J. William, I.M. Babu, G. Muralidharan, Lithium ferrite (a-$LiFe_5O_8$) nanorod based battery-type asymmetric supercapacitor with NiO nanoflakes as the counter electrode, New J. Chem. 43 (2019) 15375–15386, https://doi.org/10.1039/c9nj03774h.
[94] J. Yang, G. Zhu, Y. Liu, J. Xia, Z. Ji, X. Shen, $Fe_3O_4$-decorated $Co_9S_8$ nanoparticles in situ grown on reduced graphene oxide : a new and efficient electrocatalyst for oxygen evolution reaction, Adv. Funct. Mater. 26 (2016) 4712, https://doi.org/10.1002/adfm.201600674.
[95] Q. Gao, C.-Q. Huang, Y.-M. Ju, M.-R. Gao, J.-W. Liu, D. An, C.-H. Cui, Y.-R. Zheng, W.-X. Li, S.-H. Yu, Phase selective synthesis of unique cobalt telluride nanofleeces for highly efficient oxygen evolution catalyst, Angew. Chemie - Int. Ed. 56 (2017) 7769, https://doi.org/10.1002/anie.201701998.
[96] W. Zhao, C. Zhang, F. Geng, S. Zhuo, B. Zhang, Nanoporous hollow transition metal chalcogenide nanosheets synthesized via the anion-exchange reaction of metal hydroxides with chalcogenide ions, ACS Nano 8 (2014) 10909–10919.
[97] L. Stern, L. Feng, F. Song, X. Hu, Environmental science $Ni_2P$ as a Janus catalyst for water splitting : the oxygen evolution activity of $Ni_2P$ nanoparticles, Energy Environ. Sci. (2015) 2347–2351, https://doi.org/10.1039/c5ee01155h.